JACS
JOURNAL OF THE AMERICAN CHEMICAL SOCIETY
Article
pubs.acs.org/JACS

Carbon K-Edge X-ray Absorption Spectroscopy and Time-Dependent Density Functional Theory Examination of Metal−Carbon Bonding in Metallocene Dichlorides

Stefan G. Minasian,[†,‡] Jason M. Keith,[‡] Enrique R. Batista,*[,‡] Kevin S. Boland,[‡] Stosh A. Kozimor,*[,‡] Richard L. Martin,*[,‡] David K. Shuh,[†,*] Tolek Tyliszczak,[†] and Louis J. Vernon[‡]

[†]Lawrence Berkeley National Laboratory, Berkeley, California 94720, United States
[‡]Los Alamos National Laboratory, Los Alamos, New Mexico 87545, United States

Supporting Information

ABSTRACT: Metal−carbon covalence in $(C_5H_5)_2MCl_2$ (M = Ti, Zr, Hf) has been evaluated using carbon K-edge X-ray absorption spectroscopy (XAS) as well as ground-state and time-dependent hybrid density functional theory (DFT and TDDFT). Differences in orbital mixing were determined experimentally using transmission XAS of thin crystalline material with a scanning transmission X-ray microscope (STXM). Moving down the periodic table (Ti to Hf) has a marked effect on the experimental transition intensities associated with the low-lying antibonding $1a_1$* and $1b_2$* orbitals. The peak intensities, which are directly related to the M−(C_5H_5) orbital mixing coefficients, increase from 0.08(1) and 0.26(3) for $(C_5H_5)_2TiCl_2$ to 0.31(3) and 0.75(8) for $(C_5H_5)_2ZrCl_2$, and finally to 0.54(5) and 0.83(8) for $(C_5H_5)_2HfCl_2$. The experimental trend toward increased peak intensity for transitions associated with $1a_1$* and $1b_2$* orbitals agrees with the calculated TDDFT oscillator strengths [0.10 and 0.21, $(C_5H_5)_2TiCl_2$; 0.21 and 0.73, $(C_5H_5)_2ZrCl_2$; 0.35 and 0.69, $(C_5H_5)_2HfCl_2$] and with the amount of C 2p character obtained from the Mulliken populations for the antibonding $1a_1$* and $1b_2$* orbitals [8.2 and 23.4%, $(C_5H_5)_2TiCl_2$; 15.3 and 39.7%, $(C_5H_5)_2ZrCl_2$; 20.1 and 50.9%, $(C_5H_5)_2HfCl_2$]. The excellent agreement between experiment, theory, and recent Cl K-edge XAS and DFT measurements shows that C 2p orbital mixing is enhanced for the diffuse Hf (5d) and Zr (4d) atomic orbitals in relation to the more localized Ti (3d) orbitals. These results provide insight into how changes in M−Cl orbital mixing within the metallocene wedge are correlated with periodic trends in covalent bonding between the metal and the cyclopentadienide ancillary ligands.

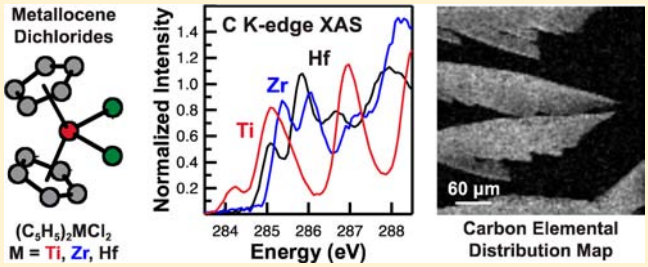

INTRODUCTION

Advancing understanding of metal−light atom (C, N, and O) electronic structure and bonding is of widespread interest because these interactions control the physics and chemistry of many important technological processes. This is especially true for systems with σ and π M−C bonds, as demonstrated in industry through polymerization of organic molecules and in nature through catalysis in organometallic reactions.[1] Non-reactive carbon-based ligands are also ubiquitous in inorganic chemistry. For example, cyclopentadienide ($C_5R_5^-$, R = H or alkyl) is a nonreactive ligand that supports a variety of reactions within metallocene wedges of $(C_5R_5)_2MX_2$ complexes (X = anion).[2−4] Cyclopentadienyl ligands provide steric stabilization and can impart desirable solubility properties, but usually do not participate directly in chemical transformations.[5] In-depth studies suggest that M−(C_5R_5) orbital mixing can also have an inductive effect on the M−X interaction,[6−12] such that changes in ring substituents can alter accompanying reaction chemistry.[13−17] However, there exist few experimental methods that can be used to quantify M−C orbital mixing in a broad range of organometallic molecules and carbon-based materials.

Seminal work by Solomon, Hedman, Hodgson, and co-workers has established ligand K-edge X-ray absorption spectroscopy (XAS) as a general technique for quantifying covalency for M−Cl and M−S bonds.[18−25] The technique probes bound state transitions between core ligand 1s and unoccupied molecular orbitals, which only have intensity if the empty acceptor orbitals contain ligand p character. In principle, C K-edge XAS can also be used to quantify M−C orbital mixing because the underlying physics governing Cl and S K-edge XAS also holds for carbon. However, the C K-edge (ca. 280 eV) is much lower in energy than that for Cl and S (>2400 eV). Thus, acquiring quantitative C K-edge XAS results is complicated by weakly penetrating incident radiation that is potentially susceptible to surface contamination and saturation effects from the samples. These technical challenges are magnified by the presence of carbon as a common contaminant, especially on synchrotron instrumentation and X-ray optics. Interpreting C K-edge XAS results for complex organometallic

Received: June 11, 2013
Published: September 18, 2013

dx.doi.org/10.1021/ja405844j | J. Am. Chem. Soc. 2013, 135, 14731−14740

systems, like $(C_5R_5)_2MX_2$, is also challenging because M−C transitions are often difficult to identify among transitions arising from ligand-based C−C and C−H bonds.[26−28]

The results provided herein show that for highly symmetric d^0 metallocenes, $(C_5H_5)_2MCl_2$ (M = Ti, Zr, Hf), the technical challenges associated with C K-edge experiments can be overcome by conducting transmission XAS measurements with a scanning transmission X-ray microscope (STXM). In addition to providing accurate pre-edge peak intensities, the STXM measurement is nondestructive and compatible with a wide range of sample types, e.g., radioactive, air-sensitive, and environmental (even extraterrestrial) specimens.[29−35] Confidence that correct C K-edge spectra were obtained using STXM was provided by the agreement of our measurements made on $(C_5H_5)_2TiCl_2$ with published inner-shell electron energy loss spectroscopy (ISEELS) measurements made on the same compound.[36] The transitions associated with the M−C, C−C, and C−H based orbitals were experimentally identified through comparison with analogous measurements made on $(C_5H_5)Na$ and further confirmed using ground-state and time-dependent hybrid density functional theory (DFT and TDDFT). Results are presented in the context of previously published Cl K-edge XAS and DFT analyses of the same $(C_5H_5)_2MCl_2$ metallocenes, which provides a consistent bonding picture from the perspective of both the ancillary $C_5H_5^-$ and reactive Cl^- ligands.[37] Together these spectroscopic and theoretical results revealed marked differences in frontier orbital compositions with variations in metal identity, which is directly related to the progressive changes in the energy and radial extension of the 3d, 4d, and 5d atomic orbitals.

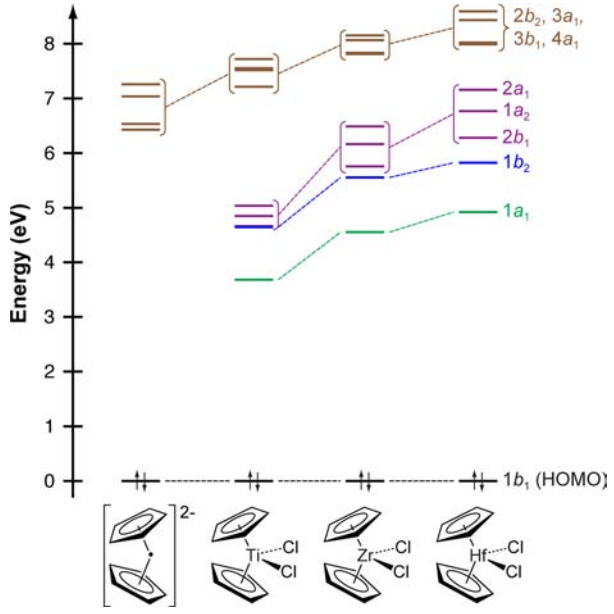

Figure 1. Quantitative molecular orbital correlation diagram for the formation of $(C_5H_5)_2MCl_2$ (M = Ti, Zr, Hf) from two $(C_5H_5)^-$ fragments in C_{2v} symmetry. Molecular orbital energies have been shifted by a constant so that each HOMO has an energy of 0 eV.

RESULTS AND DISCUSSION

Ground State Electronic Structure and Molecular Orbital Description. Before discussing the C K-edge XAS for $(C_5H_5)_2MCl_2$ in detail (M = Ti, Zr, Hf), it is instructive to provide a framework for evaluating molecular orbital interactions in each complex. Because bent metallocenes have been the subject of numerous physical investigations,[9,10,23,36−50] their electronic structures are well established.[8,12,51] As a result, this discussion will focus on metal-based unoccupied orbitals that are relevant to the C K-edge XAS experiment.

DFT calculations were conducted on $(C_5H_5)_2MCl_2$ systems whose geometries had been optimized with staggered C_5H_5 rings. The bond distances and angles were consistent with reported single-crystal X-ray diffraction studies,[52−55] and the orbital energies and compositions agreed well with previous theoretical reports.[23,37,47] To simplify electronic structure discussions, expectations from group theory were derived from $(C_5H_5)_2MCl_2$ compounds with eclipsed C_5H_5 rings in the C_{2v} point group and are summarized as follows. When the two $(C_5H_5)^-$ ligands are considered exclusively, group theory shows ten orbitals that are perpendicular to the ring planes, five of which can form bonding interactions with the metal d orbitals (Figures 1 and 2). The resulting five M−(C_5H_5) $1a_1$, $1b_2$, $2b_1$, $1a_2$, and $2a_1$ orbitals are also allowed by symmetry to mix and form σ- and π-bonds with the Cl^- wedge ligands, as shown for the antibonding orbitals in Figure 2. For these C_{2v} $(C_5H_5)_2MCl_2$ compounds, it is important to recognize that each of the a_1 orbitals contain a combination of M $d_{x^2-y^2}$ and d_{z^2} character (Figure 2).[12] As expected based on the relative energies of the 3d, 4d, and 5d atomic orbitals, the DFT calculations show an increase in energy for the unoccupied M−C antibonding $1a_1$*, $1b_2$*, $1b_1$*, $1a_2$*, and $2a_1$* orbitals with heavier metals, such that Ti < Zr < Hf. Four of the remaining five $(C_5H_5)_2^{2-}$ orbitals do not mix significantly with the metal d orbitals in C_{2v} symmetry and are best described as M−(C_5H_5) nonbonding $2b_2$, $3a_1$, $3b_1$, and $4a_1$ orbitals (Figure 1, brown). This leaves an orbital of $1b_1$ symmetry as a M−C and M−Cl nonbonding HOMO (Figure 1, black). The calculated HOMO−LUMO gaps increase from 3.68 to 4.55 to 4.92 eV for $(C_5H_5)_2MCl_2$ (M = Ti to Zr to Hf), which is similar to values obtained previously from ligand to metal charge transfer absorptions measured using optical spectroscopy (2.407, 3.668, and 3.974 eV for M = Ti, Zr, and Hf, respectively).[56]

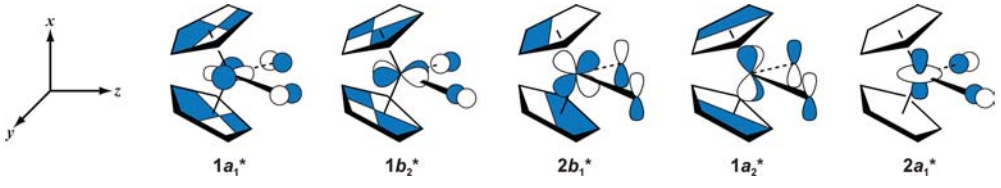

Figure 2. Antibonding interaction of metal d and ligand orbitals. The nodal characteristics of the $(C_5H_5)_2^{2-}$ fragment relative to the metal atom are represented with common short-hand notation.[12,92]

dx.doi.org/10.1021/ja405844j | J. Am. Chem. Soc. 2013, 135, 14731−14740

Carbon K-edge Measurements and Data Reduction. The STXM on the Advanced Light Source Molecular Environmental Science (ALS-MES) beamline 11.0.2 is ideally suited for accurate light atom (C, N, O, F) K-edge XAS measurements on finely divided powders.[57,58] However, for the C K-edge XAS analyses reported here, it was difficult to identify particles among mechanically ground analytes that were large enough to provide a suitable signal-to-background ratio, and also thin enough to avoid complications from saturation effects (refer to Figure S1 in the Supporting Information). An alternative sample preparation method was developed to overcome these technical challenges. In the procedure, small droplets of a solution containing the analyte dissolved in an appropriate solvent—ca. 1 mg of $(C_5H_5)_2MCl_2$ in 1 mL of toluene—were evaporated on a Si_3N_4 window in an argon filled glovebox. A majority of the resulting thin crystallites provided short pathlengths for X-ray radiation, which ensures that saturation effects are minimized and that the absorbance measurement is within the linear regime of the Beer−Lambert law. The evaporation approach also provides a straightforward and reproducible method to arrange a large number of suitable crystallites in a compact area for C K-edge XAS raster scans. Figure 3 shows representative contrast images and C elemental maps of the $(C_5H_5)_2MCl_2$ crystallites used in the C K-edge XAS experiments, light transmitted through wide regions of the crystallites (25 and 100 μm_2) was utilized to collect C K-edge spectra.

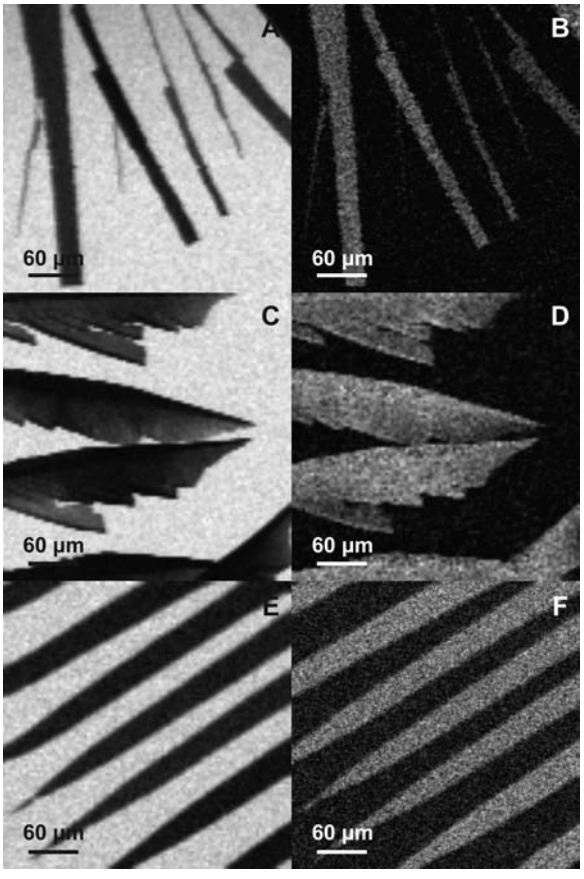

Figure 3. Two images each of the crystallites of $(C_5H_5)_2MCl_2$ (M = Ti, Zr, Hf) from which XAS were obtained: normal contrast images (left) obtained with a photon energies of 289 (Ti and Zr) and 296 eV (Hf), and elemental maps of C (right) obtained by subtraction using photon energies of 286 and 276 eV (Ti and Zr) and 280 and 290 eV (Hf) with the regions containing C shown as white using a standard grayscale. Images A and B correspond to $(C_5H_5)_2TiCl_2$, C and D to $(C_5H_5)_2ZrCl_2$, and E and F to $(C_5H_5)_2HfCl_2$.

Figure 4 shows the background subtracted and normalized C K-edge XAS spectra obtained for crystallites of $(C_5H_5)_2MCl_2$

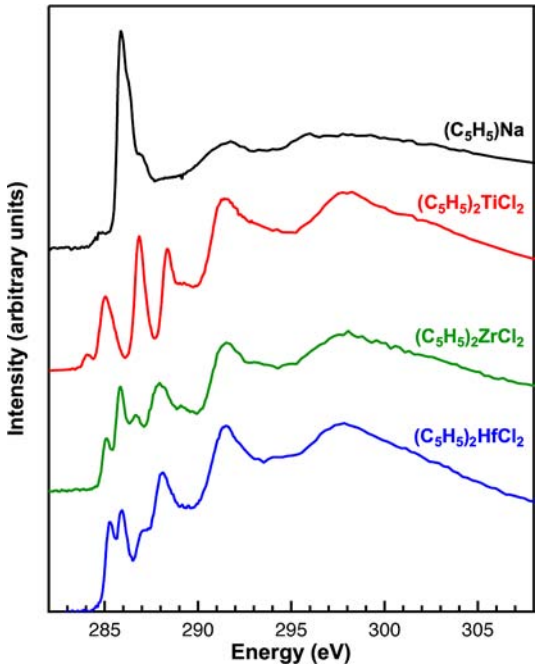

Figure 4. C K-edge XAS obtained in transmission for $(C_5H_5)Na$ (black trace), $(C_5H_5)_2TiCl_2$ (red trace), $(C_5H_5)_2ZrCl_2$ (green trace), and $(C_5H_5)_2HfCl_2$ (blue trace).

(M = Ti, Zr, Hf) and a $(C_5H_5)Na$ powder, the latter of which was used as a spectroscopic proxy for an uncoordinated $C_5H_5^-$ ligand. All spectra were measured using circularly polarized light to ensure that relative intensity changes could be evaluated quantitatively. The experimental C K-edge XAS of $(C_5H_5)Na$ contains one intense feature near 285.9 eV which is assigned to transitions into C_5H_5-based C−C antibonding molecular orbitals. Comparison with $(C_5H_5)_2MCl_2$ spectra reveals similar transitions to C_5H_5-based orbitals at approximately 1−2 eV higher energies (286.8, 287.7, and 288.0 for Ti, Zr, and Hf, respectively). These spectra contain additional low-energy features that are indicative of M d and C 2p mixing.

For $(C_5H_5)_2TiCl_2$, comparison with the previously reported ISEELS reveals nearly identical spectral profiles[36] and provides confidence in the C K-edge XAS experimental method. The XAS data differs in that the high resolving power of the ALS-MES beamline provided enhancements in fine structure. For example, in the XAS data the lowest-energy feature at 284.1 eV is resolved as a unique peak and the higher energy feature near 285 eV is asymmetric. Another notable difference is apparent at higher energy, where a feature near 288.4 eV was observed in the XAS data but was not fully resolved in the C K-edge ISEELS of $(C_5H_5)_2TiCl_2$. However, because the ISEELS spectrum did not return to baseline in this region, the presence of additional states near 288.4 eV was proposed.[36]

Moving down the periodic table to $(C_5H_5)_2ZrCl_2$ and $(C_5H_5)_2HfCl_2$, multiple pre-edge features are also apparent between 284 and 288.5 eV. These peaks are shifted to higher energy in comparison to those observed for $(C_5H_5)_2TiCl_2$,

dx.doi.org/10.1021/ja405844j | J. Am. Chem. Soc. 2013, 135, 14731−14740

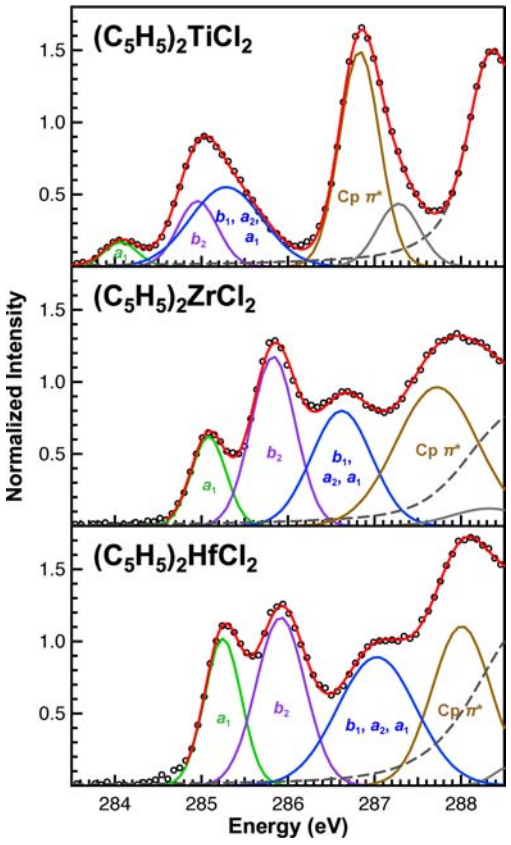

Figure 5. C K-edge XAS pre-edges (black circles) and Gaussian functions (green, purple, blue, gold, and gray traces) used to generate the curve-fits (red traces) for crystallites of $(C_5H_5)_2MCl_2$ (M = Ti, Zr, Hf). Post-edge functions have been summed and are represented by the dashed gray traces.

which is consistent with the anticipated increase in energy of the 3d, 4d, and 5d final states, respectively. Post-edge spectral profiles for all three complexes are nearly superimposable and characteristic of metallocenes. For example, the $(C_5H_5)_2MCl_2$ post-edge features resemble those in earlier ISEELS and XAS spectra recorded in total electron yield mode for linear metallocenes such as $(C_5H_5)_2M$ (M = Fe, Co, Ni).[27,28,59−63]

Spectral pre-edge features were modeled using symmetrically constrained Gaussian functions and a step function with a 1:1 ratio of arctangent and error function contributions (Figure 5 and Table 1; see also the Supporting Information). The deconvoluted $(C_5H_5)_2TiCl_2$ C K-edge spectrum, as well as the first and second derivatives of the data, suggest that the pre-edge region of the spectrum is best modeled by five Gaussian functions. Hence, the small peak near 284 eV was modeled with one low-energy function centered at 284.1 eV (green trace, Figure 5), the asymmetric peak near 285 eV with two closely spaced functions at 285.0 and 285.3 eV (purple and blue traces), and the high-energy peak near 286.9 eV with two functions at 286.8 and 287.3 eV (brown and gray traces). Using the model developed for $(C_5H_5)_2TiCl_2$ as a guide, the pre-edge features for the Zr and Hf analogues were also modeled with five functions (Figure 5 and Table 1). High-quality fits were obtained in each case as shown by good correlation coefficients, residual data that slightly deviated from zero, and symmetric residual peaks that were similar in shape to the corresponding Gaussian functions. For $(C_5H_5)_2ZrCl_2$, a fully unconstrained deconvolution did not converge with reasonable parameters for the peak height and position of the function used to model the third pre-edge feature (blue trace). To obtain a realistic model for $(C_5H_5)_2ZrCl_2$, two parameters associated with third function's peak height and position were constrained (height = 0.8, position = 286.6 eV) based on comparison with the TDDFT model (see below). Uncertainty in the area under the Gaussian functions (hereafter referred to as the intensity) due to errors in normalization or curve-fitting were estimated at less than 10% from our ability to reproduce the data.

Table 1. Comparison of Experimental and Calculated C K-Edge Pre-edge Peak Energies (eV),[a] Intensities (Int),[b] and TDDFT-Calculated Oscillator Strengths (f)[c] for $(C_5H_5)_2MCl_2$ (M = Ti, Zr, Hf)

	experimental		TDDFT	
assignment	energy (eV)	Int[b]	energy (eV)	f[c]
	$(C_5H_5)_2TiCl_2$			
$1s \rightarrow a_1$	284.1	0.08(1)	284.1	0.10
$1s \rightarrow b_2$	285.0	0.26(3)	284.8	0.21
$1s \rightarrow b_1 + a_2 + a_1$	285.3	0.57(6)	284.9	0.61
	$(C_5H_5)_2ZrCl_2$			
$1s \rightarrow a_1$	285.1	0.31(3)	285.1	0.21
$1s \rightarrow b_2$	285.8	0.75(8)	285.9	0.73
$1s \rightarrow b_1 + a_2 + a_1$	286.6	0.70(7)	286.7	0.41
	$(C_5H_5)_2HfCl_2$			
$1s \rightarrow a_1$	285.2	0.54(5)	285.2	0.35
$1s \rightarrow b_2$	285.9	0.83(8)	286.0	0.69
$1s \rightarrow b_1 + a_2 + a_1$	287.0	1.02(1)	287.2	0.79

[a]Calculated values were taken from the TDDFT simulated spectra (see Experimental Section). [b]Experimental intensities were derived from the area under Gaussian functions used to generate the curve fit and have an estimated error of less than 10%. [c]Oscillator strengths were taken from the TDDFT calculations and were scaled by the same factor for all compounds. The scale factor was based on the $(C_5H_5)_2TiCl_2$ data and determined by dividing the total experimental intensity by the sum of the TDDFT oscillator strengths for the well-resolved C 1s → $1a_1$*, C 1s → $1b_2$*, and C 1s → $2b_1$* + $1a_2$* + $2a_1$* transitions.

Pre-edge Spectral Interpretations. Carbon K-edge XAS for $(C_5H_5)_2MCl_2$ (M = Ti, Zr, Hf) were calculated using TDDFT to guide spectral interpretations of the experimental data. This approach has been applied successfully to several transition metal systems.[23,37,49,50,58,64−67] The simulated spectra for each $(C_5H_5)_2MCl_2$ compound are shown in Figure 6, and the energies and oscillator strengths of calculated transitions are given in Table 1. The TDDFT simulated spectra are consistent with expectations from group theory, which suggests that all transitions associated with spin and electric-dipole allowed $^1A_1$, $^1B_1$, or $^1B_2$ final states are allowed for C_{2v}-symmetric d^0 transition metal $(C_5H_5)_2MCl_2$ complexes. Mixing between the metal d and $(C_5H_5)_2^{2-}$ fragment orbitals results in a large number of bound-state transitions in the TDDFT calculations (>100), while only four features were resolved in the experimental C K-edge XAS spectra. To facilitate assigning spectral features to excited states associated with specific orbitals, a partial density of states (PDOS) was derived from the TDDFT by isolating contributions to each component associated with the final state $1a_1$*, $1b_2$*, $2b_1$*, $1a_2$*, $2a_1$*, and ligand orbitals (Figure 7). Each TDDFT and PDOS simulated spectrum shown in Figures 6 and 7 has been shifted (approximately +10 eV) to account for omission of atomic relaxation and other effects,[68] such that energies for the

dx.doi.org/10.1021/ja405844j | J. Am. Chem. Soc. 2013, 135, 14731−14740

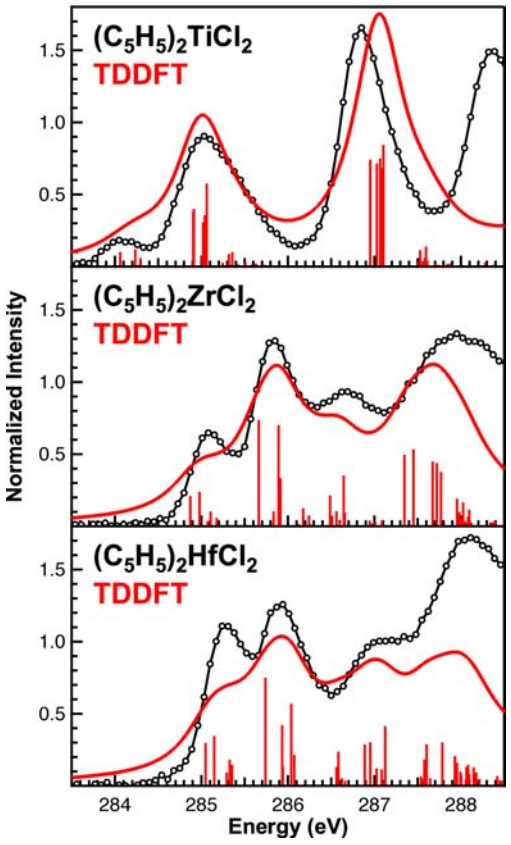

Figure 6. Carbon K-edge XAS (STXM) experimental data (black traces) for $(C_5H_5)_2MCl_2$ (M = Ti, Zr, Hf), the TDDFT-calculated spectra (red traces), and calculated transitions (red bars).

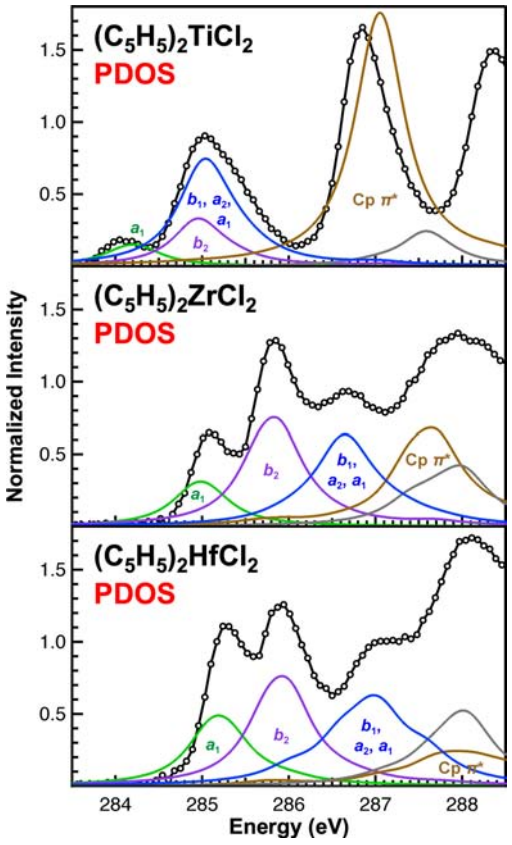

Figure 7. Experimental C K-edge XAS spectra for $(C_5H_5)_2MCl_2$ (M = Ti, Zr, Hf; black traces), and the partial density of states (PDOS) for final states associated with the $1a_1$, $1b_2$, $2b_1 + 1a_2 + 2a_1$ orbitals and M−C nonbonding C_5H_5 π^* and Rydberg-type orbitals (represented as green, purple, blue, gold, and gray traces). The absolute energies plotted for the TDDFT-calculated transitions have been shifted to account for omission of atomic relaxation and other effects[68] by aligning the calculated and experimental features associated with the C 1s → $1a_1$* LUMO transitions (see the Experimental Section).

calculated and experimental features associated with the well-resolved C 1s → $1b_2$* transitions were in alignment. The TDDFT calculations for $(C_5H_5)_2MCl_2$ show electronic excitations from C 1s orbitals into predominantly metal-based $1a_1$*, $1b_2$*, $2b_1$*, $1a_2$*, and $2a_1$* orbitals, giving rise to low-energy features whose energies and relative amplitudes are in excellent agreement with those observed in the experimental spectra (Table 1).

Each of the TDDFT calculations for the C K-edge XAS for $(C_5H_5)_2MCl_2$ exhibits a cluster of low-energy electronic excitations and suggests that the first features in the experimental spectra are associated with closely spaced transitions from C 1s-based orbitals to the low-lying $1a_1$* LUMOs. The TDDFT calculations also indicate that the second features are associated entirely with the d orbitals of $1b_2$* symmetry, and that the third features arise from a band of overlapping transitions from the C 1s orbitals to the remaining metal d orbitals of $2b_1$*, $1a_2$*, and $2a_1$* symmetry. Resolving these transitions was not possible, as evident from attempts to incorporate additional Gaussian functions into the curve fits of the experimental spectra, which provided peak heights and widths with high error bars. As alluded to above, the fourth features are attributed to transitions from C 1s orbitals into the higher-lying C_5H_5-based $3a_1$*, $2a_2$*, $3b_1$*, and $2b_2$* molecular orbitals (Figure 1). These orbitals are essentially M−(C_5H_5) nonbonding in rigorous C_{2v} symmetry, and transition intensity in this region is not reflective of M−(C_5H_5) orbital mixing. Consistent with several other ligand K-edge studies,[36,49,57,58,67,69] the calculations predict additional transitions to higher lying Rydberg-type orbitals that may account for the fifth low-intensity and high-energy features in the experimental spectra (Figures 5 and 7, solid gray traces).

Additional support for the spectral interpretations was obtained by comparing the TDDFT-calculated spectra for $(C_5H_5)_2TiCl_2$ and an idealized C_{2v} $(C_5H_5)_2^{2-}$ fragment (Figure 8). Transitions into the C_5H_5-based C−C antibonding molecular orbitals for C_{2v} $(C_5H_5)_2^{2-}$ were observed near 286.5 eV, which suggests that the lower energy features in the experimental and TDDFT-calculated C K-edge XAS of

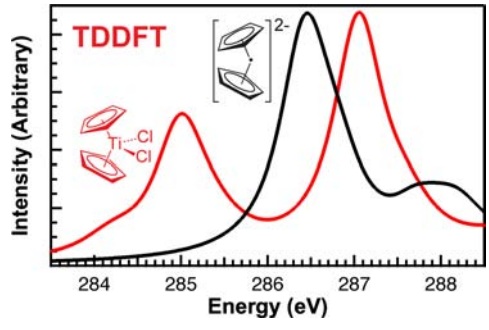

Figure 8. TDDFT simulated spectra for $(C_5H_5)_2TiCl_2$ (red trace) and an idealized C_{2v} $(C_5H_5)_2^{2-}$ fragment (black trace).

dx.doi.org/10.1021/ja405844j | J. Am. Chem. Soc. 2013, 135, 14731−14740

$(C_5H_5)_2TiCl_2$ are associated with M−C interactions. The C K-edge peak energies and splittings were also compared to those determined previously at the Cl K-edge for the same Group 4 metallocenes, $(C_5H_5)_2MCl_2$ (M = Ti, Zr, Hf; Figure 9).[23,37,49]

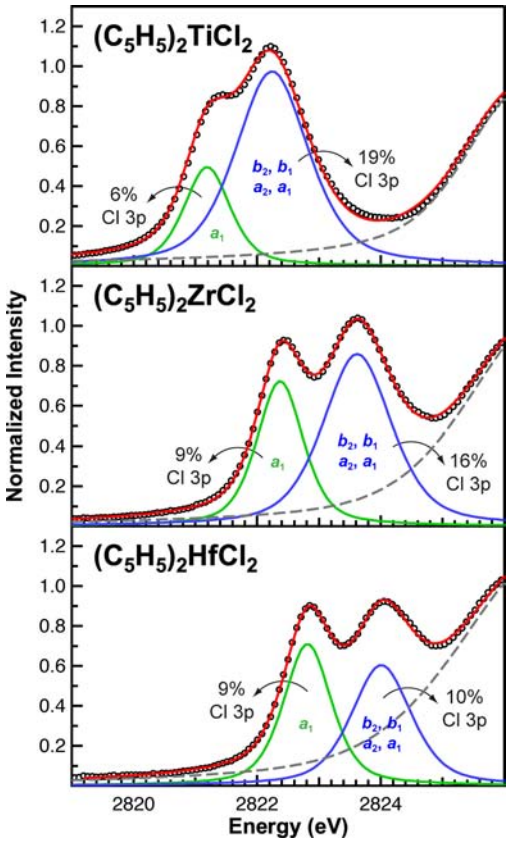

Figure 9. Cl K-edge XAS pre-edges (black circles) and Gaussian functions (green and blue traces) used to generate the curve-fits (red traces) for polystyrene film samples of $(C_5H_5)_2MCl_2$ (M = Ti, Zr, Hf). Adapted with permission from ref 37. Copyright 2008 American Chemical Society.

Each of the previously reported experimental Cl K-edge spectra exhibited two features: one at low energy attributed to Cl 1s → $1a_1$* excitations, and another at higher energy assigned to a band of overlapping excitations into the remaining $1b_2$*, $2b_1$*, $1a_2$*, and $2a_1$* orbitals. For spectra obtained on samples dispersed as thin films on kapton tape, the splittings between these two features were 1.04, 1.18, and 1.11 eV for M = Ti, Zr, and Hf, respectively.[37] These values compare well with the splittings between the C 1s → $1a_1$* features and the weighted average of the two C 1s → $1b_2$* and C 1s → $2b_1$* + $1a_2$* + $2a_1$* features, as determined from the experimental C K-edge XAS (1.12, 1.13, and 1.28 eV for Ti, Zr, and Hf) and the TDDFT (0.82, 1.14, and 1.39 eV, for Ti, Zr, and Hf).

Evaluating M−(C_5H_5) Bonding. Because the C K-edge pre-edge transitions described above have intensities that are weighted by the amount of C 2p character in the molecular orbitals, they can be used to evaluate relative changes in M−(C_5H_5) orbital mixing for $(C_5H_5)_2MCl_2$ with metals from different rows of the periodic table. For all $(C_5H_5)_2MCl_2$, the pre-edge features associated with the $1a_1$* antibonding orbital were evaluated using the curve-fitting analysis described above, which yields increasing intensities from 0.08 to 0.31 to 0.54 for M = Ti, Zr, and Hf, respectively (Table 1). It is worth highlighting that these relative increases are substantial, such that C 2p character in the $1a_1$* orbitals increases by a factor of 3.8 on moving from Ti to Zr and by an additional 1.7 from Zr to Hf. Comparable increases in pre-edge peak intensity were also observed for the transitions associated with the higher-lying $1b_2$* orbitals of $(C_5H_5)_2TiCl_2$ and $(C_5H_5)_2ZrCl_2$, which have intensities of 0.26 and 0.75, respectively, relative to 0.83 for $(C_5H_5)_2HfCl_2$. These values suggest that C 2p character in the $1b_2$* orbitals increases by a factor of 2.9 from Ti to Zr, and by 1.1 from Zr to Hf. The total intensity measured for the overlapping transitions to the remaining three $2b_1$*, $1a_2$*, and $2a_1$* orbitals increased modestly between different metallocenes: the area under the curve fit associated with transitions to the $2b_1$*, $1a_2$*, and $2a_1$* antibonding orbitals was 0.57, 0.70, and 1.02 for $(C_5H_5)_2TiCl_2$, $(C_5H_5)_2ZrCl_2$, and $(C_5H_5)_2HfCl_2$, which corresponds to increases in C 2p character by factors of 1.2 and 1.5 from Ti to Zr and Zr to Hf, respectively.

The intensities measured in transmission XAS using the STXM suggest that the amount of M−(C_5H_5) mixing is appreciably larger for the heavier transition metals, particularly in the low-lying $1a_1$* and $1b_2$* orbitals. Relative changes in the oscillator strengths calculated using TDDFT are in excellent agreement with this experimental observation (Table 1). To facilitate direct comparisons between the experimental and calculated data, the raw TDDFT-calculated oscillator strengths for all $(C_5H_5)_2MCl_2$ were adjusted by a scaling factor. This factor was based on the $(C_5H_5)_2TiCl_2$ data and determined by dividing the total experimental intensity by the sum of the TDDFT oscillator strengths for the well-resolved C 1s → $1a_1$*, C 1s → $1b_2$*, and C 1s → $2b_1$* + $1a_2$* + $2a_1$* transitions (Table 1). As observed experimentally, the TDDFT shows a substantial increase in the intensity of the low-energy C 1s → $1a_1$* and C 1s → $1b_2$* transitions with $(C_5H_5)_2MCl_2$ based on second- and third-row metals ($1a_1$* = 0.10, 0.21, 0.35, and $1b_2$* = 0.21, 0.73, and 0.69 for M = Ti, Zr, and Hf, respectively). The combination of overlapping transitions into the $2b_1$*, $1a_2$*, and $2a_1$* orbitals also resulted in a large feature in each of the TDDFT-calculated spectra with intensities totaling 0.61, 0.41, and 0.79 eV for M = Ti, Zr, and Hf, respectively, which is in line with the experimental data.

As described above, the C K-edge XAS transition intensities provided from the transmission XAS and TDDFT data establish a framework for understanding the excited state electronic structure changes between different $(C_5H_5)_2MCl_2$ molecules. For example, the magnitude of the changes in XAS and TDDFT-calculated transition intensities are also consistent with the trends in C 2p orbital mixing coefficients associated with the respective eigenvectors as demonstrated by comparison with the Mulliken analyses (Table 2 and Figure 10). These calculations show that the percentage of C 2p character in the $1a_1$* LUMO is 8.2% for $(C_5H_5)_2TiCl_2$, which nearly doubles on moving to $(C_5H_5)_2ZrCl_2$ (15.3% C 2p), and increases by an additional factor of 1.3 for $(C_5H_5)_2HfCl_2$ (20.1% C 2p). A comparable increase in C 2p mixing was calculated for the $1b_2$* orbital, beginning at 23.4% for $(C_5H_5)_2TiCl_2$, increasing by a factor of 1.7−39.7% for $(C_5H_5)_2ZrCl_2$, and rising again by a factor of 1.3−50.9% for $(C_5H_5)_2HfCl_2$. Only modest changes are anticipated in the remaining antibonding $2b_1$*, $1a_2$*, $2a_1$* orbitals, which have total C 2p characters of 71.8, 67.7, and 76.9% for M = Ti, Zr, and Hf, respectively.

dx.doi.org/10.1021/ja405844j | J. Am. Chem. Soc. 2013, 135, 14731−14740

Table 2. Calculated Energies[a] and Atomic Compositions[b] of Selected Valence Molecular Orbitals for $(C_5H_5)_2MCl_2$ (M = Ti, Zr, Hf)

		MO (DFT, %)				
MO	energy (eV)	M s	M p	M d	C 2p	Cl 3p
		$(C_5H_5)_2TiCl_2$				
$2a_1$*	−1.39	0.0	0.6	72.1	19.9	6.0
$1a_2$*	−1.58	0.0	0.0	69.9	27.5	1.4
$2b_1$*	−1.76	0.0	1.1	70.9	24.4	1.8
$1b_2$*	−1.78	0.0	0.3	57.8	23.4	17.6
$1a_1$*	−2.74	0.0	0.5	76.5	8.2	13.2
$1b_1$	−6.42	0.0	0.3	7.1	55.0	36.2
		$(C_5H_5)_2ZrCl_2$				
$2a_1$*	−0.18	0.8	3.4	71.9	17.4	5.0
$1a_2$*	−0.50	0.0	0.0	67.8	27.6	2.6
$2b_1$*	−0.91	0.0	4.8	68.2	22.7	2.4
$1b_2$*	−1.11	0.0	0.0	47.9	39.7	11.6
$1a_1$*	−2.11	0.0	1.4	69.1	15.3	12.4
$1b_1$	−6.66	0.0	0.4	5.7	66.9	25.3
		$(C_5H_5)_2HfCl_2$				
$2a_1$*	0.55	2.1	23.0	52.5	12.6	3.4
$1a_2$*	0.16	0.3	0.0	57.3	37.1	2.6
$2b_1$*	−0.33	0.0	7.5	60.8	27.2	2.0
$1b_2$*	−0.79	0.0	−0.2	39.7	50.9	8.5
$1a_1$*	−1.69	0.1	1.6	63.5	20.1	11.2
$1b_1$	−6.61	0.0	0.3	5.1	69.2	23.8

[a]Alpha spin−orbital energies are reported. [b]The use of a non-orthogonal basis set can cause Mulliken analysis to have non-physical results such as compositions >100% or <0.[93] For each molecule, the lowest energy MO is the non-bonding highest occupied molecular orbital (HOMO).

CONCLUDING REMARKS

The results presented in this study have shown that accurate carbon K-edge peak intensities can be measured with transmission XAS and used to identify experimental trends in M−C orbital mixing for transition metal organometallics. Pre-edge features associated with transitions to each of the metal d orbitals were observed in the carbon K-edge XAS and TDDFT of $(C_5H_5)_2MCl_2$ (M= Ti, Zr, Hf), and both experiment and theory strongly agree that M *n*d and C 2p orbital mixing increases with the increasing principle quantum number (n) of the d orbitals. Combined, the results indicate that the total C 2p character increases by a factors of 1.9 (XAS) or 1.5 (TDDFT) from M = Ti to Zr and by an additional 1.4 (XAS and TDDFT) from M = Zr to Hf. Particularly large increases were observed for transitions into the low-lying $1a_1$* LUMO, where C 2p character was observed to jump by a factor of 6.7 (XAS) or 3.5 (TDDFT) from $(C_5H_5)_2TiCl_2$ to $(C_5H_5)_2HfCl_2$. These increases suggests that the $1a_1$* LUMO is more localized on Ti for $(C_5H_5)_2TiCl_2$, and that M−(C_5H_5) covalency is enhanced significantly for Zr and Hf. Smaller increases in C 2p character were observed in the higher-lying $2b_1$*, $1a_2$*, and $2a_1$* orbitals, which are somewhat less nodal π- and σ-type antibonding interactions.

In earlier ISEELS, XAS, and DFT studies on $TiCl_4$, $(C_5H_5)TiCl_3$, and $(C_5H_5)_2TiCl_2$, substituting the Cl^- ligands in $TiCl_4$ with $C_5H_5^-$ ligands was found to interfere with Ti 3d−4p hybridization and reduce the amount of Ti 3d and Cl 3p orbital mixing in the wedge of $(C_5H_5)_2TiCl_2$.[23,36,49] Taken together with the C K-edge XAS measurements described here—and considering previously published Cl K-edge XAS studies on the same Group 4 $(C_5H_5)_2MCl_2$ (Figure 9)[37]—a complex interplay between M−(C_5H_5) and M−Cl bonding emerges. Moving down the Group 4 triad from Ti to Hf, M−Cl mixing in the wedge decreases by nearly one-half in the four higher-lying $1b_1$*, $2b_1$*, $1a_2$*, and $2a_1$* orbitals combined, while M−(C_5H_5) mixing more than doubles. However, M−(C_5H_5) and M−Cl mixing are not always mutually exclusive. For example, a drop in the amount of M d character from $(C_5H_5)_2TiCl_2$ to $(C_5H_5)_2HfCl_2$ accommodates increases in both Cl 3p and C 2p character in the $1a_1$* LUMO. Because the 4d and 5d orbitals are higher in energy, the increase in M−(C_5H_5) mixing for $(C_5H_5)_2ZrCl_2$ and $(C_5H_5)_2HfCl_2$ relative to $(C_5H_5)_2TiCl_2$ is most likely indicative of a pronounced improvement in spatial overlap between the C 2p and diffuse Zr 4d and Hf 5d orbitals. This improvement in overlap is not effectively offset by the increasingly less favorable energy mismatch between the C 2p and higher energy d orbitals, and leads to an overall increase in mixing that is reflected by more intense transitions to the $1a_1$* and $1b_2$* orbitals for the second- and third-row metallocenes.[67]

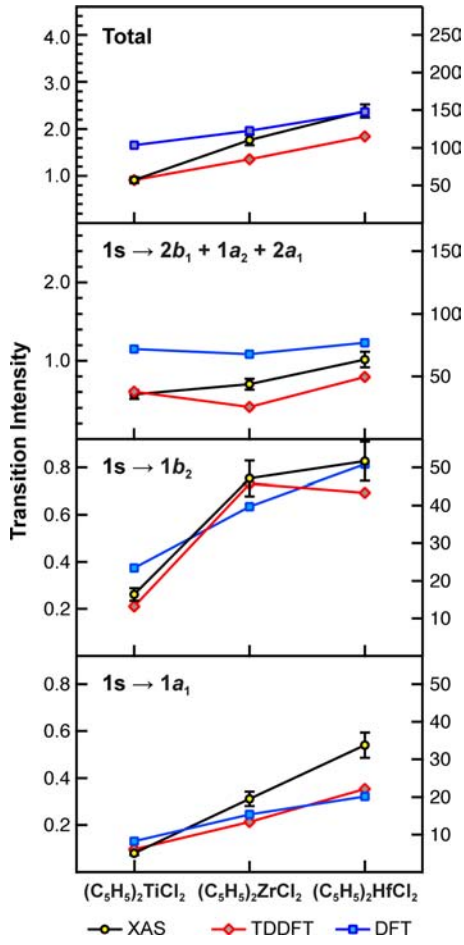

Figure 10. Comparison of XAS and TDDFT-calculated intensities (left axis, black and red traces) for transitions into the $1a_1$, $1b_2$, combined $2b_1$, $1a_2$, and $2a_1$ orbitals. The sum of the transition intensities is shown in the top panel. Carbon 2p characters (%) from the ground state DFT calculation are plotted along the right axis (blue traces). The relative scaling for the right and left *y*-axes was estimated based on the $(C_5H_5)_2HfCl_2$ experimental pre-edge peak intensity for the C 1s → $1b_2$* transition (0.83) and the amount of C 2p character in the $1b_2$* orbital determined by DFT (50.9%) given in Tables 1 and 2.

dx.doi.org/10.1021/ja405844j | J. Am. Chem. Soc. 2013, 135, 14731−14740

These studies show that $C_5H_5^-$ ligands do not behave as consistent and rigid partners for the metals in bent metallocenes; rather, their ability to engage in covalent interactions varies. The changes in M−(C_5H_5) orbital mixing observed as the Group 4 triad is descended has consequences both for interactions with ligands in the metallocene wedge and for the energy and composition of frontier orbitals. Correlations between this finding and known differences in the nucleophilicity and reactivity of bent metallocenes, e.g., $(C_5H_5)_2TiX_2$ relative to $(C_5H_5)_2ZrX_2$ and $(C_5H_5)_2HfX_2$,[70−77] will be the subject of future research.

EXPERIMENTAL SECTION

STXM Sample Preparation. All manipulations were performed with rigorous exclusion of air and moisture using Schlenk and glovebox techniques under an argon atmosphere. Toluene (Fisher) was distilled from sodium metal and benzophenone prior to use. Samples of $(C_5H_5)_2TiCl_2$, $(C_5H_5)_2ZrCl_2$, and $(C_5H_5)_2HfCl_2$ were obtained from Strem, recrystallized from toluene, and dried in *vacuo* prior to use. A small amount of each sample (∼1 mg) was dissolved in toluene (1 mL), and 0.5 μL of this solution was transferred to a Si_3N_4 window (100 nm, Silson) using a micropipet. The toluene was allowed to evaporate over a few seconds, which deposited thin crystallites of the sample on the Si_3N_4 membrane. After drying for several more minutes, a second window was placed over the sample, essentially sandwiching the crystallites, and the windows were sealed together using Hardman Double/Bubble epoxy.

Carbon K-Edge STXM Measurements. STXM methodology was similar to that discussed previously.[57,58,78−80] Single-energy images and carbon K-edge XAS spectra were acquired using the STXM instrument at the Advanced Light Source-Molecular Environmental Science (ALS-MES) beamline 11.0.2, which is operated in topoff mode at 500 mA, in a ∼0.5 atm He-filled chamber. An energy calibration was performed at the C K-edge for CO_2 gas (294.95 eV). For these measurements, the X-ray beam was focused with a zone plate onto the sample, and the transmitted light was detected. The spot size and spectral resolution were determined from characteristics of the 25 nm zone plate. Images at a single energy were obtained by raster-scanning the sample and collecting transmitted monochromatic light as a function of sample position. Spectra at each image pixel or particular regions of interest on the sample image were extracted from the "stack", which is a collection of images recorded at multiple, closely spaced photon energies across the absorption edge.[81] This enabled spatial mapping of local chemical bonding information. Dwell times used to acquire an image at a single photon energy were ∼1 ms per pixel. To quantify the absorbance signal, the measured transmitted intensity (I) was converted to optical density using Beer−Lambert's law: OD = $\ln(I/I_0) = \mu\rho d$, where I_0 is the incident photon flux intensity, d is the sample thickness, and μ and ρ are the mass absorption coefficient and density of the sample material, respectively. Incident beam intensity was measured through the sample-free region of the Si_3N_4 windows. Spectra were then obtained by averaging over the crystallites deposited on the substrate. Regions of particles with an absorption of >1.5 OD were omitted to ensure the spectra were in the linear regime of the Beer−Lambert law. The energy resolution was determined to be 0.04 eV, and spectra were collected using circularly polarized radiation. During the STXM experiment, samples showed no sign of radiation damage, and each spectrum was reproduced from multiple independent crystallites. Salient features of the spectra were reproducible using samples prepared from nonoriented polycrystalline particles.

Data Analysis. The data were normalized in MATLAB using the MBACK algorithm,[82] and by setting the edge jump at 295 eV to an intensity of 1.0. Fits to the C K-edges were performed using the program IGOR 6.0 and a modified version of EDG_FIT.[83] Second-derivative spectra were used as guides to determine the number and position of peaks. Pre-edge and rising edge features were modeled by Gaussian line shapes and a step function. For the step function, a 1:1 ratio of arctangent and error function contributions was employed. Fits were performed over several energy ranges. Assignment of merit for the curve fit was given by inspection of the residual intensity, which is obtained by subtracting the fit from the experiment and should resemble a horizontal line at zero (see Supporting Information). The area under the pre-edge peaks (defined as the intensity) is equal to the fwhm×ph (fwhm = full width at half-maximum height (eV); ph = peak height (normalized intensity). Using the sample preparation methodology discussed above, the reported pre-edge intensities were reproduced with a standard deviation of less than 10%.

Electronic Structure Calculations. Ground state electronic structure calculations were performed on the $(C_5H_5)_2MCl_2$ complexes using B3LYP hybrid density functional theory (DFT)[84,85] in the Gaussian 09 code.[86] Ti, Zr, and Hf were modeled with the effective core potential of Hay and Wadt (LANL2DZ)[87] augmented with the addition of f-polarization functions (exponents = 1.506, 0.875, and 0.784).[88] C and H were modeled using a Pople style double-ζ 6-31G(d′,p′) basis set with polarization functions optimized for heavy atoms.[89] These functionals and basis sets have demonstrated good agreement between experimental and simulated ligand K-edge XAS for organometallic and inorganic systems.[50,57,58,66] The molecular orbital compositions of each compound were obtained by Mulliken population analysis of the individual molecular orbitals.

Simulated C K-Edge Spectra. For the $(C_5H_5)_2MCl_2$ compounds, the C K-edge XAS were simulated using time-dependent density functional theory (TDDFT). These calculations were conducted as described previously.[37,50,57] Specifically, this analysis involves a linear response calculation generating the transition densities and transition dipoles between the calculated excited states and the ground states.[90] The excitations originating from all of the intermediate states between the C 1s and the HOMO were excluded so that only excitations from the core levels to virtual molecular orbitals could be analyzed. This allows the virtual orbitals to mix and reflect the presence of the carbon core hole. Relaxations for the other occupied orbitals associated with the core hole are not included. Although excluding relaxations in the occupied orbitals associated with the core hole results in large errors associated with absolute calculated transition energies, this computational technique addresses the first order changes in virtual orbitals accompanying the core hole excitation. As discussed previously,[50] an energy shift must be established to account for the omission of the atomic relaxation associated with the core excitation, relativistic stabilization, and errors associated with the functional. This was achieved by shifting the calculated energies for the especially well-resolved 1s → $1b_2$* transitions so that they were equivalent to those measured in the experimental spectra, which resulted in energy shifts of +10.09, +10.30, and +10.17 eV for $(C_5H_5)_2TiCl_2$, $(C_5H_5)_2ZrCl_2$, and $(C_5H_5)_2HfCl_2$, respectively. While natural transition orbital analysis was performed to validate the individual excitations,[91] the complex systems contained well over 100 transitions in a small energetic window (Figure 6). Hence, to facilitate assigning various spectral features to excited states associated with specific orbitals, a partial density of states (PDOS) was derived from the TDDFT by isolating contributions to each excited state from excitations into a specific virtual molecular orbital, and plotting the contributions separately (Figure 7). While these graphical representations of the PDOS provided valuable guidance for spectral assignments, quantitative oscillator strengths were derived directly from the TDDFT output (Table 1).

ASSOCIATED CONTENT

Supporting Information

Additional X-ray absorption spectra and analysis; complete refs 34, 58, and 86. This material is available free of charge via the Internet at http://pubs.acs.org.

AUTHOR INFORMATION

Corresponding Authors

erb@lanl.gov
stosh@lanl.gov

rlmartin@lanl.gov
dkshuh@lbl.gov

Notes

The authors declare no competing financial interest.

■ ACKNOWLEDGMENTS

This work was supported under the Heavy Element Chemistry Program at LANL by the Division of Chemical Sciences, Geosciences, and Biosciences, Office of Basic Energy Sciences, U.S. Department of Energy, and at LBNL by the Director, Office of Science, Office of Basic Energy Sciences, Division of Chemical Sciences, Geosciences, and Biosciences of the U.S. Department of Energy (contract DE-AC02-05CH11231). Beamline 11.0.2 at the Advanced Light Source was supported by the Director, Office of Science, Office of Basic Energy Sciences Division of Chemical Sciences, Geosciences, and Biosciences; and the Condensed Phase and Interfacial Molecular Sciences Program of the aforementioned Division of the U.S. Department of Energy at LBNL under Contract No. DE-AC02-05CH11231. The Advanced Light Source is supported by the Director, Office of Science, Office of Basic Energy Sciences, of the U.S. Department of Energy under Contract No. DE-AC02-05CH11231. Parts of this work were supported at LBNL by the Berkeley Actinide Postdoctoral Fellowship (S.G.M.), and at LANL by Glenn T. Seaborg Institute Postdoctoral Fellowships (S.G.M.) and Director's Postdoctoral Fellowships (J.M.K.). Los Alamos National Laboratory is operated by Los Alamos National Security, LLC, for the National Nuclear Security Administration of U.S. Department of Energy (contract DE-AC52-06NA25396).

■ REFERENCES

(1) Crabtree, R. H. In *The Organometallic Chemistry of the Transition Metals*, 4th ed.; John Wiley & Sons: Hoboken, NJ, 2005; p 31.
(2) Green, J. C. *Chem. Soc. Rev.* **1998**, *27*, 263.
(3) Erker, G.; Kehr, G.; Frohlich, R. *Coord. Chem. Rev.* **2006**, *250*, 36.
(4) Chirik, P. J. *Organometallics* **2010**, *29*, 1500.
(5) Evans, W. J.; Davis, B. L. *Chem. Rev.* **2002**, *102*, 2119.
(6) Ballhausen, C.; Dahl, J. P. *Acta Chem. Scand.* **1961**, *15*, 1333.
(7) Alcock, N. W. *J. Chem. Soc. A* **1967**, 2001.
(8) Green, J. C.; Green, M. L. H.; Prout, C. K. *Chem. Commun.* **1972**, 421.
(9) Condorelli, G.; Fragala, I.; Centineo, A.; Tondello, E. *J. Organomet. Chem.* **1975**, *87*, 311.
(10) Petersen, J. L.; Dahl, L. F. *J. Am. Chem. Soc.* **1975**, *97*, 6416.
(11) Petersen, J. L.; Lichtenberger, D. L.; Fenske, R. F.; Dahl, L. F. *J. Am. Chem. Soc.* **1975**, *97*, 6433.
(12) Lauher, J. W.; Hoffmann, R. *J. Am. Chem. Soc.* **1976**, *98*, 1729.
(13) La Pierre, H. S.; Arnold, J.; Bergman, R. G.; Toste, F. D. *Inorg. Chem.* **2012**, *51*, 13334.
(14) Knobloch, D. J.; Lobkovsky, E.; Chirik, P. J. *J. Am. Chem. Soc.* **2010**, *132*, 10553.
(15) Chirik, P. J.; Bercaw, J. E. *Organometallics* **2005**, *24*, 5407.
(16) Miller, S. A.; Bercaw, J. E. *Organometallics* **2004**, *23*, 1777.
(17) Pool, J. A.; Lobkovsky, E.; Chirik, P. J. *J. Am. Chem. Soc.* **2003**, *125*, 2241.
(18) Hedman, B.; Hodgson, K. O.; Solomon, E. I. *J. Am. Chem. Soc.* **1990**, *112*, 1643.
(19) Shadle, S. E.; Hedman, B.; Hodgson, K. O.; Solomon, E. I. *Inorg. Chem.* **1994**, *33*, 4235.
(20) Shadle, S. E.; Hedman, B.; Hodgson, K. O.; Solomon, E. I. *J. Am. Chem. Soc.* **1995**, *117*, 2259.
(21) Neese, F.; Hedman, B.; Hodgson, K. O.; Solomon, E. I. *Inorg. Chem.* **1999**, *38*, 4854.
(22) Glaser, T.; Hedman, B.; Hodgson, K. O.; Solomon, E. I. *Acc. Chem. Res.* **2000**, *33*, 859.
(23) George, S. D.; Brant, P.; Solomon, E. I. *J. Am. Chem. Soc.* **2005**, *127*, 667.
(24) Solomon, E. I.; Hedman, B.; Hodgson, K. O.; Dey, A.; Szilagyi, R. K. *Coord. Chem. Rev.* **2005**, *249*, 97.
(25) Sarangi, R.; George, S. D.; Rudd, D. J.; Szilagyi, R. K.; Ribas, X.; Rovira, C.; Almeida, M.; Hodgson, K. O.; Hedman, B.; Solomon, E. I. *J. Am. Chem. Soc.* **2007**, *129*, 2316.
(26) Hitchcock, A. P.; Newbury, D. C.; Ishii, I.; Stohr, J.; Horsley, J. A.; Redwing, R. D.; Johnson, A. L.; Sette, F. *J. Chem. Phys.* **1986**, *85*, 4849.
(27) Ruhl, E.; Hitchcock, A. P. *J. Am. Chem. Soc.* **1989**, *111*, 5069.
(28) Hitchcock, A. P.; Wen, A. T.; Ruhl, E. *Chem. Phys.* **1990**, *147*, 51.
(29) Yang, Y.; Saiers, J. E.; Xu, N.; Minasian, S. G.; Tyliszczak, T.; Kozimor, S. A.; Shuh, D. K.; Barnett, M. O. *Environ. Sci. Technol.* **2012**, *46*, 5931.
(30) Moffet, R. C.; Henn, T. R.; Tivanski, A. V.; Hopkins, R. J.; Desyaterik, Y.; Kilcoyne, A. L. D.; Tyliszczak, T.; Fast, J.; Barnard, J.; Shutthanandan, V.; Cliff, S. S.; Perry, K. D.; Laskin, A.; Gilles, M. K. *Atmos. Chem. Phys.* **2010**, *10*, 961.
(31) Armbruster, M. K.; Schimmelpfennig, B.; Plaschke, M.; Rothe, J.; Denecke, M. A.; Klenze, R. *J. Electron Spectrosc. Relat. Phenom.* **2009**, *169*, 51.
(32) Ade, H.; Stoll, H. *Nat. Mater.* **2009**, *8*, 281.
(33) Baldea, I.; Schimmelpfennig, B.; Plaschke, M.; Rothe, J.; Schirmer, J.; Trofimov, A. B.; Fanghanel, T. *J. Electron Spectrosc. Relat. Phenom.* **2007**, *154*, 109.
(34) Sandford, S. A.; et al. *Science* **2006**, *314*, 1720.
(35) Nilsson, H. J.; Tyliszczak, T.; Wilson, R. E.; Werme, L.; Shuh, D. K. *Anal. Bioanal. Chem.* **2005**, *383*, 41.
(36) Wen, A. T.; Hitchcock, A. P. *Can. J. Chem.* **1993**, *71*, 1632.
(37) Kozimor, S. A.; Yang, P.; Batista, E. R.; Boland, K. S.; Burns, C. J.; Christensen, C. N.; Clark, D. L.; Conradson, S. D.; Hay, P. J.; Lezama, J. S.; Martin, R. L.; Schwarz, D. E.; Wilkerson, M. P.; Wolfsberg, L. E. *Inorg. Chem.* **2008**, *47*, 5365.
(38) Petersen, J. L.; Dahl, L. F. *J. Am. Chem. Soc.* **1975**, *97*, 6422.
(39) Bassobert, M.; Cassoux, P.; Crasnier, F.; Gervais, D.; Labarre, J.; Deloth, P. *J. Organomet. Chem.* **1977**, *136*, 201.
(40) Cauletti, C.; Clark, J. P.; Green, J. C.; Jackson, S. E.; Fragala, I. L.; Ciliberto, E.; Coleman, A. W. *J. Electron Spectrosc. Relat. Phenom.* **1980**, *18*, 61.
(41) Fragala, I.; Marks, T. J.; Fagan, P. J.; Manriquez, J. M. *J. Electron Spectrosc. Relat. Phenom.* **1980**, *20*, 249.
(42) Kenney, J. W.; Boone, D. R.; Striplin, D. R.; Chen, Y. H.; Hamar, K. B. *Organometallics* **1993**, *12*, 3671.
(43) King, W. A.; Di Bella, S.; Gulino, A.; Lanza, G.; Fragala, I. L.; Stern, C. L.; Marks, T. J. *J. Am. Chem. Soc.* **1999**, *121*, 355.
(44) Langmaier, J.; Samec, Z.; Varga, V.; Horacek, M.; Mach, K. *J. Organomet. Chem.* **1999**, *579*, 348.
(45) Loukova, G. V. *Chem. Phys. Lett.* **2002**, *353*, 244.
(46) Zachmanoglou, C. E.; Docrat, A.; Bridgewater, B. M.; Parkin, G.; Brandow, C. G.; Bercaw, J. E.; Jardine, C. N.; Lyall, M.; Green, J. C.; Keister, J. B. *J. Am. Chem. Soc.* **2002**, *124*, 9525.
(47) Wang, X. J.; Chen, L.; Endou, A.; Kubo, M.; Miyamoto, A. *J. Organomet. Chem.* **2003**, *678*, 156.
(48) Ray, K.; George, S. D.; Solomon, E. I.; Wieghardt, K.; Neese, F. *Chem.—Eur. J.* **2007**, *13*, 2783.
(49) Casarin, M.; Finetti, P.; Vittadini, A.; Wang, F.; Ziegler, T. *J. Phys. Chem. A* **2007**, *111*, 5270.
(50) Kozimor, S. A.; Yang, P.; Batista, E. R.; Boland, K. S.; Burns, C. J.; Clark, D. L.; Conradson, S. D.; Martin, R. L.; Wilkerson, M. P.; Wolfsberg, L. E. *J. Am. Chem. Soc.* **2009**, *131*, 12125.
(51) Bruce, M. R. M.; Kenter, A.; Tyler, D. R. *J. Am. Chem. Soc.* **1984**, *106*, 639.
(52) Tkachev, V. V.; Atovmyan, L. O. *Zh. Strukt. Khim.* **1972**, *13*, 287.

(53) Prout, K.; Cameron, T. S.; Forder, R. A. *Acta Crystallogr. B* **1974**, *30*, 2290.
(54) Clearfield, A.; Warner, D. K.; Saldarriagamolina, C. H.; Ropal, R.; Bernal, I. *Can. J. Chem.* **1975**, *53*, 1622.
(55) Soloveichik, G. L.; Arkhireeva, T. M.; Bel'skii, V. K.; Bulychev, B. M. *Metalloorg. Khim.* **1988**, *1*, 226.
(56) Loukova, G. V.; Strelets, V. V. *J. Organomet. Chem.* **2000**, *606*, 203.
(57) Bradley, J. A.; Yang, P.; Batista, E. R.; Boland, K. S.; Burns, C. J.; Clark, D. L.; Conradson, S. D.; Kozimor, S. A.; Martin, R. L.; Seidler, G. T.; Scott, B. L.; Shuh, D. K.; Tyliszczak, T.; Wilkerson, M. P.; Wolfsberg, L. E. *J. Am. Chem. Soc.* **2010**, *132*, 13914.
(58) Minasian, S. G.; et al. *J. Am. Chem. Soc.* **2013**, *135*, 1864.
(59) Ruhl, E.; Wen, A. T.; Hitchcock, A. P. *J. Electron Spectrosc. Relat. Phenom.* **1991**, *57*, 137.
(60) Wen, A. T.; Ruhl, E.; Hitchcock, A. P. *Organometallics* **1992**, *11*, 2559.
(61) Otero, E.; Wilks, R. G.; Regier, T.; Blyth, R. I. R.; Moewes, A.; Urquhart, S. G. *J. Phys. Chem. A* **2008**, *112*, 624.
(62) Otero, E.; Kosugi, N.; Urquhart, S. G. *J. Chem. Phys.* **2009**, *131*, 114313.
(63) Otero, E.; Shipman, P. O.; Abd-El-Aziz, A. S.; Urquhart, S. G. *Organometallics* **2009**, *28*, 2160.
(64) George, S. D.; Petrenko, T.; Neese, F. *Inorg. Chim. Acta* **2008**, *361*, 965.
(65) George, S. D.; Neese, F. *Inorg. Chem.* **2010**, *49*, 1849.
(66) Daly, S. R.; Keith, J. M.; Batista, E. R.; Boland, K. S.; Clark, D. L.; Kozimor, S. A.; Martin, R. L. *J. Am. Chem. Soc.* **2012**, *134*, 14408.
(67) Minasian, S. G.; Keith, J. M.; Batista, E. R.; Boland, K. S.; Christensen, C. N.; Clark, D. L.; Conradson, S. D.; Kozimor, S. A.; Martin, R. L.; Schwarz, D. E.; Shuh, D. K.; Wagner, G. L.; Wilkerson, M. P.; Wolfsberg, L. E.; Yang, P. *J. Am. Chem. Soc.* **2012**, *134*, 5586.
(68) Segala, M.; Chong, D. P. *J. Electron Spectrosc. Relat. Phenom.* **2010**, *182*, 141.
(69) Fillaux, C.; Guillaumont, D.; Berthet, J.-C.; Copping, R.; Shuh, D. K.; Tyliszczak, T.; Den Auwer, C. *Phys. Chem. Chem. Phys.* **2010**, *12*, 14253.
(70) Breslow, D. S.; Newburg, N. R. *J. Am. Chem. Soc.* **1957**, *79*, 5072.
(71) Gladysz, J. A. *Chem. Rev.* **2000**, *100*, 1167.
(72) Toney, J. H.; Brock, C. P.; Marks, T. J. *J. Am. Chem. Soc.* **1986**, *108*, 7263.
(73) Allen, O. R.; Croll, L.; Gott, A. L.; Knox, R. J.; McGowan, P. C. *Organometallics* **2004**, *23*, 288.
(74) Allen, O. R.; Knox, R. J.; McGowan, P. C. *Dalton Trans.* **2008**, 1293.
(75) Kostova, I. *Anti-Cancer Agents Med. Chem.* **2009**, *9*, 827.
(76) Tshuva, E. Y.; Ashenhurst, J. A. *Eur. J. Inorg. Chem.* **2009**, 2203.
(77) Pizarro, A. M.; Habtemariam, A.; Sadler, P. J. In *Medicinal Organometallic Chemistry*; Jaouen, G.Metzler-Nolte, N., Eds.; Springer: Berlin, 2010; Vol. *32*, p 21.
(78) Minasian, S. G.; Krinsky, J. L.; Rinehart, J. D.; Copping, R.; Tyliszczak, T.; Janousch, M.; Shuh, D. K.; Arnold, J. *J. Am. Chem. Soc.* **2009**, *131*, 13767.
(79) Bugaris, D. E.; Choi, E. S.; Copping, R.; Glans, P.-A.; Minasian, S. G.; Tyliszczak, T.; Kozimor, S. A.; Shuh, D. K.; Ibers, J. A. *Inorg. Chem.* **2011**, *50*, 6656.
(80) Gianetti, T. L.; Nocton, G.; Minasian, S. G.; Tomson, N. C.; Kilcoyne, A. L. D.; Kozimor, S. A.; Shuh, D. K.; Tyliszczak, T.; Bergman, R. G.; Arnold, J. *J. Am. Chem. Soc.* **2013**, *135*, 3224.
(81) Hitchcock, A. P. *aXis*, V. 17-Sep-08; McMaster University: Hamilton, Ontario, Canada, 1908.
(82) Weng, T. C.; Waldo, G. S.; Penner-Hahn, J. E. *J. Synchrotron Radiat.* **2005**, *12*, 506.
(83) George, G. N. *EDG_FIT*; Stanford Synchrotron Radiation Laboratory, Stanford Linear Accelerator Center: Stanford, CA.
(84) Becke, A. D. *J. Chem. Phys.* **1993**, *98*, 5648.
(85) Lee, C. T.; Yang, W. T.; Parr, R. G. *Phys. Rev. B* **1988**, *37*, 785.
(86) Frisch, M. J.; et al. *Gaussian09*, Revision B.01; Wallingford, CT.
(87) Hay, P. J.; Wadt, W. R. *J. Chem. Phys.* **1985**, *82*, 299.
(88) Ehlers, A. W.; Bohme, M.; Dapprich, S.; Gobbi, A.; Hollwarth, A.; Jonas, V.; Kohler, K. F.; Stegmann, R.; Veldkamp, A.; Frenking, G. *Chem. Phys. Lett.* **1993**, *208*, 111.
(89) Petersson, G. A.; Bennett, A.; Tensfeldt, T. G.; Allaham, M. A.; Shirley, W. A.; Mantzaris, J. *J. Chem. Phys.* **1988**, *89*, 2193.
(90) Elliott, P.; Furche, F.; Burke, K. In *Reviews in Computational Chemistry*; Lipkowitz, K. B., Cundari, T. R., Eds.; Wiley: Hoboken, NJ, 2009; p 91.
(91) Martin, R. L. *J. Chem. Phys.* **2003**, *118*, 4775.
(92) Albright, T. A.; Burdett, J. K.; Whangbo, M. *Orbital Interactions in Chemistry*; John Wiley and Sons: New York, 1985.
(93) Cramer, C. J. *Essentials of Computational Chemistry*, 2nd ed.; Wiley: Chichester, UK, 2004.